VISUALIZATION OF UNSTEADY FLOW IN A MULTISTAGE HELICO-AXIAL PUMP

T. Ø. S. Gundersen[1,3,]* ⓘ *- V. Moënne-Loccoz[2] - M. Dupoiron[2]*
E. A. Torbergsen[3] - B. Balakin[4] ⓘ *- B. J. Arntzen[1] - A. C. Hoffmann[1]* ⓘ

[1]Department of Physics and Technology, University of Bergen, Norway
[2]IFP Energies nouvelles, Solaize, France
[3]OneSubsea, an SLB company, Bergen, Norway
[4]Western Norway University of Applied Sciences, Bergen, Norway
[*]Corresponding author: ted.gundersen@uib.no

ABSTRACT

Helico-axial pumps are designed to pump mixtures of gas and liquid. Secondary flows and rotor-stator interactions are known to add complexity to the flow field in unshrouded axial-flow turbomachinery. Here we use a high-speed camera to visualize the internal flow field in a multistage helico-axial pump. A wide range of relative flow rates are investigated to see how secondary flows emerge and evolve depending on the operating point. Nitrogen bubbles are used as tracers to obtain a qualitative understanding of the flow. The recordings exhibit a highly unsteady flow field that varies with the relative flow rate. The tip leakage flow and interactions between the components lead to recirculation and reversed flow, also when operating near the best efficiency point. Local gas accumulation and stagnant fluid was observed near the impeller outlet at very low relative flow rate, where the slope of the head-flow curve had shifted.

KEYWORDS

helico-axial pump, flow visualization, experiment, secondary flows, multiphase

NOMENCLATURE

A_1	Cross-sectional area at impeller inlet
b_1	Blade height at impeller inlet
dp	Pump differential static pressure
$GVF = Q_g/Q$	Gas volume fraction
g	Gravitational constant
$H = dp/\rho g$	Pump head
$N = \Omega Q^{\frac{1}{2}}/(gH)^{\frac{3}{4}}$	Specific speed
Q_g	Actual volumetric gas flow rate
Q_l	Actual volumetric liquid flow rate
$Q = Q_l + Q_g$	Actual volumetric flow rate
R_T	Impeller tip radius
$Re_T = 2\rho\Omega R_T^2/\mu$	Tip-speed Reynolds number
s	Impeller tip radial clearance
μ	Fluid dynamic viscosity
ρ	Fluid density
$\phi = Q/A_1 R_T \Omega$	Flow coefficient
ϕ_{BEP}	Flow coefficient at pump's best efficiency point
$\psi = dp/\rho R_T^2 \Omega^2$	Head coefficient
Ω	Radian frequency of shaft rotation

INTRODUCTION

Rotodynamic pumps with helico-axial compression cells are designed to pump mixtures of gas and liquid, for example when boosting an incoming well stream of oil and gas. The compression cell consists of an axial-flow impeller and diffuser where the blade height is relatively small compared to the impeller tip diameter. The impeller is unshrouded to avoid any accumulation of solids and the blades resemble a section of a helix. Secondary flows can have a significant impact on the internal flow field, and in a multistage setup, rotor-stator interaction adds further complexity and unsteadiness to the flow. Experimental data is essential to improve our understanding and characterize the internal flow in these pumps.

Several studies have been conducted to investigate the flow field in inducers. As for helico-axial impellers, inducers are unshrouded and have high-solidity blades. Lakshminarayana (1982) and Brennen (2011) describe an internal flow field based on visualization experiments, where secondary flows and shear forces play an integral part. The tip leakage flow contributes to backflow upstream of the inducer inlet and radial velocities within the inducer, that are in the same order of magnitude as the axial velocities. The dynamics of the backflow with and without cavitation, as well as other inducer instabilities, have been studied in detail, see e.g. Tsujimoto et al. (2005) and d'Agostino (2013). More recently, Mansour et al. (2019) investigated the influence of an inducer installed upstream of a centrifugal impeller operating under multiphase conditions. Cavitation and impact of the tip leakage flow in other types of hydraulic machinery have been studied in several publications, see Serena & Bakken (2015) and the review by Cheng et al. (2021). For axial compressors, the tip leakage flow has been linked to stall inception (Tan et al. 2010, Yamada et al. 2013).

For helico-axial pumps, a setup suitable for flow visualization and laser Doppler velocimetry experiements has previously been commissioned as described by El Hajem et al. (2003).

Vilagines et al. (2003) tested a single stage and indicate a periodic internal flow field with significant prerotation upstream the impeller due to the tip leakage flow. Vilagines et al. (2004) tested the same compression cell in a multistage setup and found a performance reduction for the first stage compared to the second and third stage, due to the different inlet conditions. The tests were conducted in single phase conditions, near the best efficiency point (BEP). Internal pressure and velocity components were measured by intrusive pressure probes. They indicated backflow related to the impeller tip leakage flow near the shroud, as well as a strong correlation between the diffuser flow pattern and the passing of the downstream impeller blade. Also the impeller outlet conditions were affected by the presence of a downstream impeller. Since commercial pumps with helico-axial compression cells typically consist of several stages in series, it is thus important to study a stage with both an upstream and downstream stage to improve global pump performance predictions.

Another experimental setup with a transparent pump casing has been used to investigate varying multiphase flow regimes in a three-stage configuration with helico-axial compression cells, as described by Zhang et al. (2016) and others. The flow field is described as very complicated, with large vortices observed in the diffuser channels, sometimes causing reversed flow.

In the present study we use a high-speed camera to study the flow field in a pump comprising three low-specific speed helico-axial compression stages. A small amount of gas is injected in the liquid to visualize that the internal flow field in the second stage is unsteady and that secondary flows emerge and evolve as the flow rate is varied over a wide range. The purpose is to obtain qualitative results that can also be useful in validation and improvement of numerical modeling techniques.

EXPERIMENTAL SETUP
Helico-Axial Visualization Rig
The experiments were conducted with the Helico-Axial Visualization Rig (HAVR). The rig, flowloop and instrumentation are described in Gundersen et al. (2022). The rig's pump unit contained three identical helico-axial compression stages in an axial setup during the experiments. The pump casing was transparent and a water-filled visualization box was installed on the casing to facilitate flow visualization with a high-speed camera. The camera used in the present study was a Photron FASTCAM APX-RS high-speed camera with a Nicon Micro-Nikkor $60\,\mathrm{mm}$ f/2.8D lens. The camera was connected to a computer through ethernet and operated in the Photron FASTCAM Viewer software. Lighting was provided by a ProPhotonix Cobra Max LED Line Light installed in a vertical position. Two additional LED panels distributed a more diffuse light at the area of interest. A photo of the setup can be seen in figure 1.

Pump Characteristics
The helico-axial compression cell installed in HAVR was a 50% scaled version of a full-scale design. The specific speed at the best efficiency point is relatively low for an axial design, $N = 0.72$ for one full-scale cell in a multistage setup, in single phase conditions. Figure 2 illustrates the second compression stage installed in HAVR, together with a cross-sectional view of the fluid domain where the fluid flows vertically upwards through the pump.

The impellers were machined in stainless steel material with a specified maximum surface roughness of $1.6\,\mu\mathrm{m}$. The surface was treated with a black-oxide finish to facilitate for the flow visualization experiments. The diffusers were 3D-printed in a black polymer material and
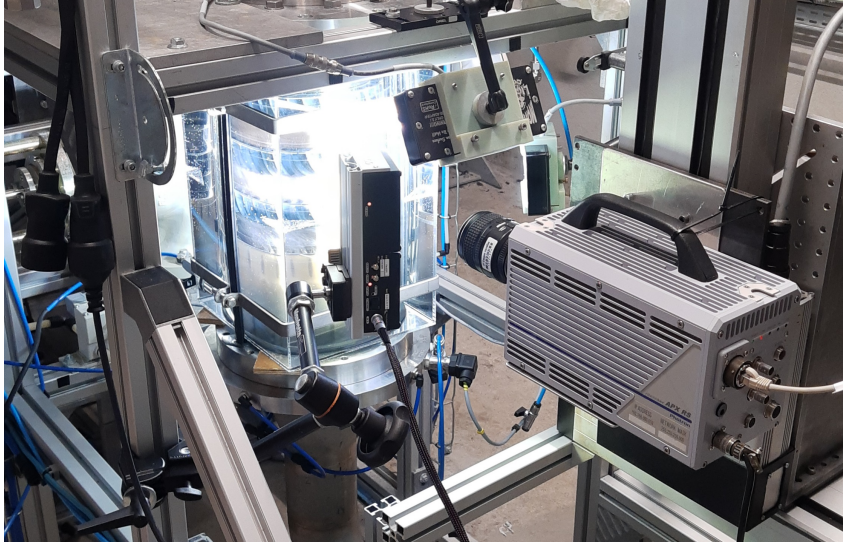
Figure 1: Experimental setup with LED lights and a high-speed camera, focusing on the transparent pump unit where a water-filled visualization box is installed.

manually sanded to reduce the surface roughness, yielding a roughness of approximately $9\,\mu$m. Note that the diffuser has a small ring at the outer diameter of the trailing edge, outside the flow path. The ring supports the vanes in the diffuser assembly and creates a small obstruction to the view of the diffuser outlet. Geometric properties of the compression cell are given in table 1. Further details including performance assessment can be found in Gundersen et al. (2022).

Impeller tip radius R_T	$82.5\,\mathrm{mm}$
Number of impeller blades	4
Impeller blade tip inlet angle	$3.7°$
Impeller radial tip clearance s/b_1	3.7%
Number of diffuser vanes	23
Diffuser vane thickness	$2\,\mathrm{mm}$

Table 1: Helico-axial compression cell geometric properties

Operating Conditions

High-speed videos were recorded at different relative flow rates ϕ/ϕ_{BEP} and can be found in the referenced dataset Gundersen et al. (2023). For the present results, the pump was operated at $1500\,\mathrm{rpm}$ and the fluid was fresh water with a small amount of nitrogen injected at the pump inlet. For each recording, the relevant flow rate was obtained in single phase conditions before the temporary gas injection was initiated. The gas was injected through a thermal mass flow controller that kept the inlet gas volume fraction (GVF) constant during each recording. The liquid and gas phases were mixed in the pump, directly upstream of the inlet guide vanes. Any large nitrogen bubbles were broken down in the first impeller due to shear and turbulence. The video recordings focus on the pump's second compression cell, where the bubbles act as tracers to describe the flow field. The GVF varied somewhat between the recordings, within the range of 0.3% to 1.7%. The pump suction pressure and temperature were $1.5\,\mathrm{bara}$ and $23\,°\mathrm{C}$,
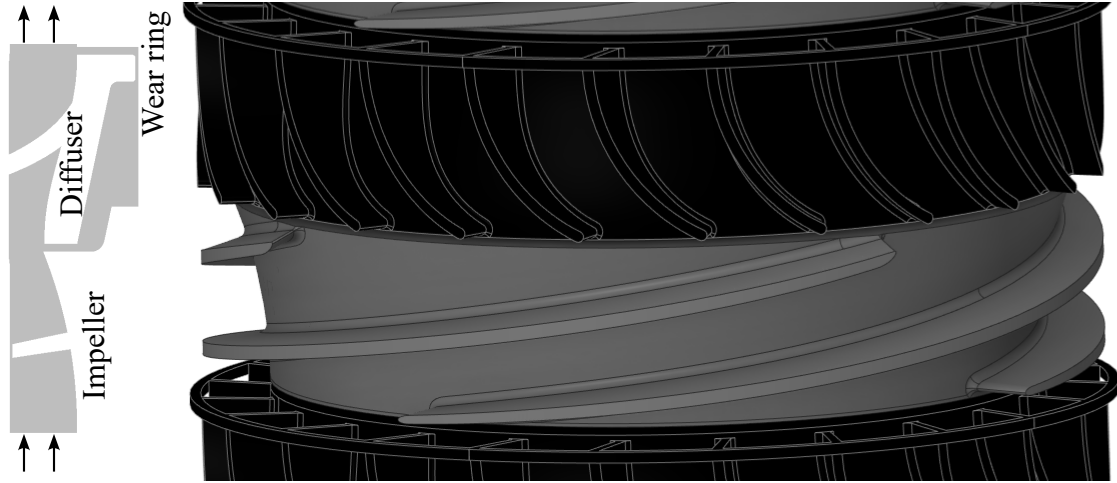
Figure 2: Illustration of the second helico-axial compression cell in HAVR, including cross-sectional view of its fluid domain. Arrows indicate the inlet and outlet of the cell.

respectively. The tip-speed Reynolds number Re_T was 2.3×10^6 in single phase water. Videos were recorded at 5000 frames per second, with a resolution of 512×1024 pixels.

Figure 3 provides an overview of the relative flow rate and GVF for each recording presented. The relative flow rate varies from 133% to 45%. The flow visualization conditions are shown relative to the the pump's single phase head characteristic, represented by two best-fit polynomials based on data points documented in Gundersen et al. (2022). Any deviation from the characteristic reflects the measured effect on pump head (i.e. efficacy) when introducing the nitrogen. The multiphase fluid density used to calculate head is based on the volumetric average at the pump outlet. It is seen that ψ is practically unaffected at these low gas volume fractions, with the exception of the lowest relative flow rate. This will be discussed subsequently.
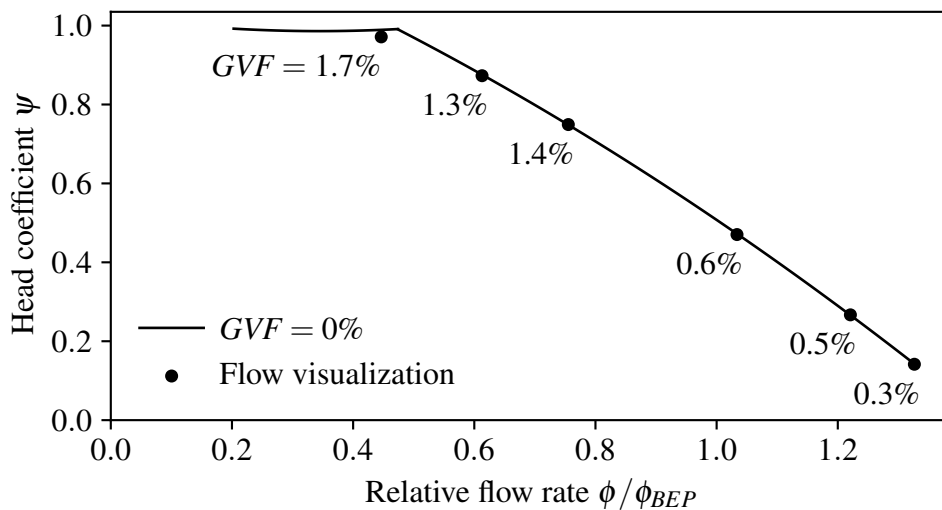

Figure 3: Overview of flow visualization recordings exhibited in the present paper. Operating conditions are shown relative to the single-phase head characteristic. The gas volume fraction (GVF) is indicated for each recording.

FLOW VISUALIZATION

Recordings are presented to illustrate how the characterstics of the flow evolve with varying operating conditions. We study the flow field as we move from high to low relative flow rates ϕ/ϕ_{BEP}. The general figure in the current section exhibits an image from the high-speed recordings. The left-hand side of the figure displays the image including overlaid shroud and hub contours for the diffuser vanes. The contours are added to ease the interpretation of the image. A copy of the image is shown on the right-hand side of the figure, wherein properties of the flow are emphasized.
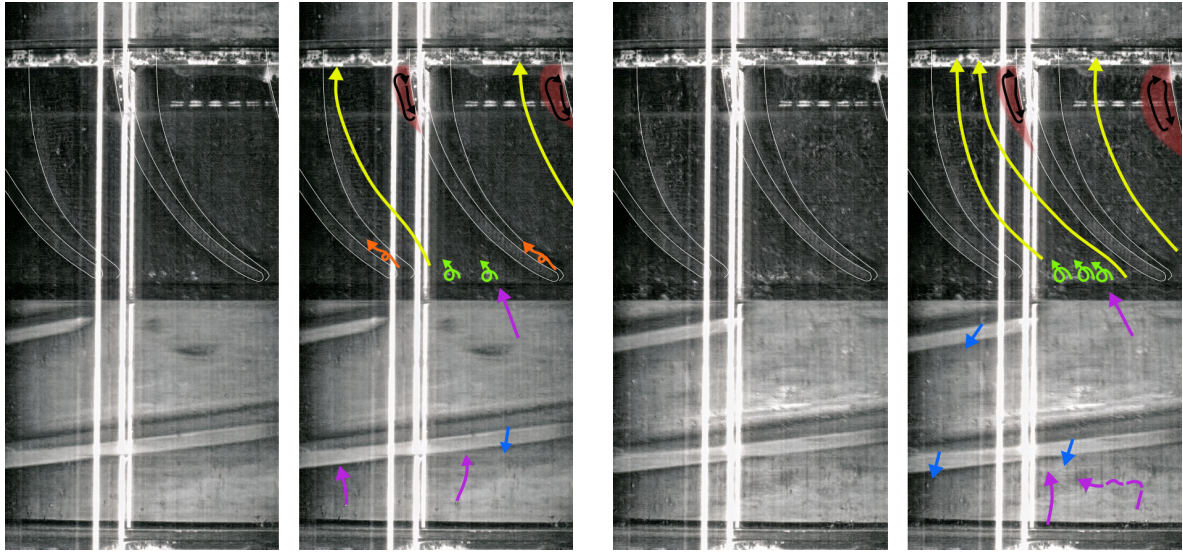
High Relative Flow Rates

Figure 4a shows a frame recorded at 133% relative flow rate. Relatively large bubbles (normally up to $0.5\,\mathrm{mm}$) enter the impeller from the upstream diffuser. The purple arrows illustrate segments of bubble trajectories in the impeller, in the stationary frame of reference. The flow is predominantly axial in the impeller. Near the outlet however, a small tangential velocity component was observed. Although the differential pressure is small, tip leakage flow from the pressure to the suction side of the impeller blades can still be observed at different locations along the circumference. The tip leakage flow is indicated by blue arrows in the figures.

An accumulation of bubbles can be observed at the diffuser inlet, in the middle passage in figure 4a. They are indicated by green arrows on the right-hand side of figure 4a. The accumulation was intermittent and related to the periodic passing of the upstream impeller blade trailing edge, also seen in the figure; At some instances, flow separation from the diffuser inlet hub surface occured as the impeller trailing edge passed and caused a pressure fluctuation in this area. Within a period of $2\,\mathrm{ms}$, bubbles remained in a small recirculation zone before the flow reattached and the bubbles were transported further downstream. The diffuser inlet is prone to flow separation at the hub due to the abrupt change in hub curvature relative to the upstream impeller outlet, see figure 2. Additionally, any fluid exiting the diffuser wear ring domain adds a radial outward velocity component to the flow that promotes detachment from the hub.

A minor and sporadic flow separation was observed directly downstream the diffuser leading edge, on the pressure side of the vanes (orange arrows in figure 4a). This is attributed to the negative incidence angle obtained at this high relative flow rate. Generally, the fluid passes through the diffuser without signs of significant secondary flows. Yellow arrows represent typical flow paths for bubbles entering the diffuser. Towards the outlet however, a zone of more stagnant fluid was observed on the suction side of the diffuser vanes. The area is indicated by semi-transparent red color in the figures. A clockwise recirculation pattern was observed within the zone. Apparently, the boundary layer at the suction side of the vanes separated from the surface under the adverse pressure gradient arising from the increase in effective flow area through the diffuser.

Figure 4b shows the flow at 122% relative flow rate. The overall flow field is similar to that seen in figure 4a, with an overall steady and predominantly axial flow in the impeller. The influence of the tip leakage flow is however becoming visible, with examples of bubbles being entrained and exhibiting nearly stagnant axial velocity near the shroud in the middle of the blade passage (dashed purple arrow). At the diffuser inlet, the periodic separation at the hub is now more prominent and visible along the circumference of the channel as each impeller trailing edge passes. Still, the flow reattaches between each blade pass. At the diffuser outlet, the reduced flow rate results in separation further upstream and an increased size of the

(a) Flow visualization at 133% relative flow rate **(b) Flow visualization at 122% relative flow rate**

Figure 4: Flow visualization at high relative flow rates

recirculation zone which is effectively reducing the streamwise flow area. The recirculating fluid motion within this zone exhibits an increased periodicity related to the passing of the downstream impeller blades.

Near Design Point

As the relative flow rate is reduced and the pump operates near BEP, the internal flow field becomes more complex with significant secondary flows and coherent structures. Figure 5 was recorded at 103% relative flow rate and exhibits a more three-dimensional flow field relative to the higher flow rates. Stronger shear forces are now contributing to break-up of bubbles and somewhat reduced bubble sizes.
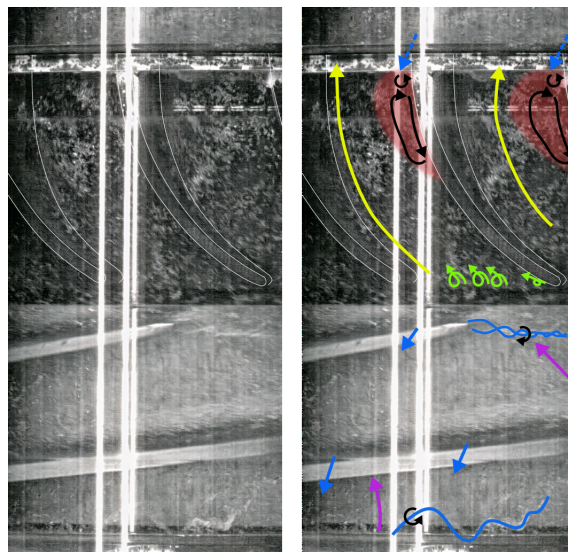

Figure 5: Flow visualization at 103% relative flow rate

As the differential pressure increases, the impeller tip leakage flow rate also increases. An impeller tip leakage vortex (TLV) emerged behind the leading edge of the impeller and is indicated by a blue line. It is seen that the vortex core propagates axially and can reach upstream of the impeller inlet plane. The axial propagation can be attributed to the incoming flow from the upstream diffuser. A serpentine shape of the TLV appears due to the circumferential variation in momentum of the diffuser outlet flow near the shroud. The TLV is advected upstream by the tip leakage flow near the outlet recirculation zone, while it can be axially stagnant or advected downstream where the outlet flow velocity is high.

The serpentine shape is broken as the next impeller blade leading edge divides the TLV. Remnants of the TLV can however remain stable and affect the downstream flow pattern. Some were identified as they were transported through the impeller where they could span the core of the channel. An example of this is illustrated in figure 6. Some vortices remained visible until they left the impeller, contributing to the unsteady diffuser inlet conditions. Finally, an impeller trailing edge tip vortex was also identified. The vortex dissipates and disappears rather quickly.
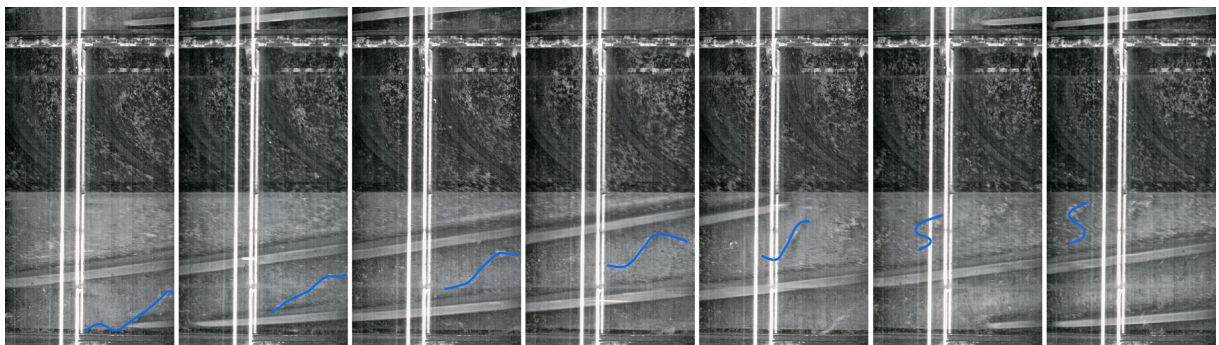

Figure 6: Example of evolution of tip leakage vortex in impeller channel at 103% relative flow rate. Part of the vortex is tracked with a blue line. Time duration between each frame is 2 ms.

The periodic separation at the diffuser inlet hub was still present at 103% relative flow rate and was now accompanied by a periodic flow separation from the suction side of the diffuser vane, directly behind the leading edge (green arrows). Further downstream in the diffuser, the detachment point related to the outlet recirculation zone moved axially closer to the middle of the channel. A spanwise variation in velocity can be identified directly downstream of this point. Reversed flow can be seen close to the hub, while positive streamwise velocity is seen near the shroud. This implies that the recirculation zone is initiated by corner separation at the root of the vanes.

A small counterclockwise recirculation pattern has emerged near the diffuser trailing edge, coexisting with the larger clockwise recirculation. This is attributed to the downstream impeller tip leakage flow that reaches into the outlet section, i.e. impeller backflow. The backflow contains a tangential velocity component (see the dashed blue arrows) and drives the counterclockwise motion near the shroud on the suction side of the vane.

Low Relative Flow Rates

Figure 7a displays the flow field when the volumetric flow rate was reduced below the design point to 76% relative flow rate. The TLV and its serpentine shape has become more prominent as the impeller tip leakage increases with higher differential pressure. At the impeller inlet,

the purple arrow illustrates how some bubbles entering axially were traced to the suction side of the blade, where they moved radially towards the impeller tip and were entrained in the tip leakage flow. After moving axially downwards a certain distance, most bubbles entered the core of the impeller flow again. At this operating condition, the radial outward velocity component along both the pressure and suction side of the impeller blades was visible. This is in line with the description of secondary flows in inducers given by Lakshminarayana (1982) and Brennen (2011). Note that the radial velocity along the blade is considered beneficial for the helico-axial impeller's multiphase operation capabilities. Generally it will counteract accumulation of gas that is drawn towards the suction side of the blade or the hub. The gas is entrained in the liquid-rich tip leakage flow coming from the pressure side of the blade and the phases are subsequently homogenized within the core of the impeller channel.

At the diffuser inlet, the detachment from the hub has become permanent; Reversed flow was observed along a section of the hub, indicated by red arrows in figure 7a. At the inlet of the diffuser, bubbles traveling upstream with the reversed flow were entrained in the impeller outlet flow (yellow arrows) and transported downstream again. Near the outlet, the counterclockwise recirculation pattern has grown considerably due to the increased impeller backflow. A smaller counterclockwise recirculation zone was also established on the pressure side of the vane. The incoming fluid in the diffuser channel is deflected in between the two zones and partially inwards towards the hub before it enters the downstream impeller.
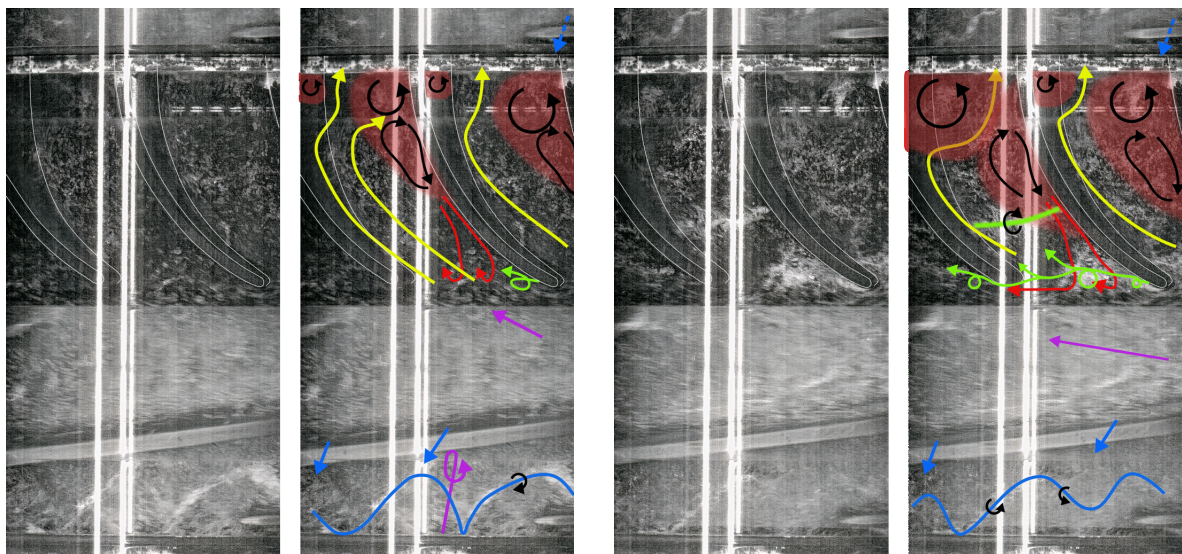
(a) **Flow visualization at 76% relative flow rate**   (b) **Flow visualization at 61% relative flow rate**

Figure 7: Flow visualization at low relative flow rates

Further reduction of the pump inlet flow rate to 61% of BEP results in a highly unsteady and more chaotic internal flow, as seen in figure 7b. At the diffuser inlet, there were instances of significant vortex shedding from the leading edge of the vane (green arrow). This vortex would often interact with reversed flow along the hub. The reversed flow in the diffuser exhibited a stronger periodicity corresponding to the impeller blade passing frequency, where the axial velocity varied between almost stagnant and a significant negative value. Some of the incoming fluid that separated from the diffuser leading edge was unable to enter the diffuser channel, possibly related to the periodic reversed flow and passing of the downstream impeller blade. The

fluid was deflected and transported circumferentially to the next channel where a new diffuser leading edge separation vortex was formed due to the high incidence angle. A majority of the fluid from the impeller would however enter the channel and could trigger the formation of a horizontal vortex in the shear layer between the reversed flow and the streamwise flow closer to the shroud. This characteristic vortex (green line in figure 7b) could span most of the diffuser channel circumferentially and was sustained by the shear layer. It was advected downstream in the channel towards the outlet recirculation zones, where it was distorted and broken down.

The flow pattern at the outlet of the diffuser was unsteady at the current relative flow rate; The strong impeller backflow resulted in irregular shifting between one large and two smaller counterclockwise recirculation zones in the diffuser channel outlet. The two patterns are represented in figure 7b. Both patterns entail a significant deflection of the streamwise flow which to a large degree is forced to enter the impeller away from the shroud.

The lowest relative flow rate considered in this study is 45% of BEP, as seen in figure 8. The pump operating point was just beyond where the head-flow curve is no longer increasing when further reducing the flow rate, as seen in figure 3. It is thus outside what would normally be defined as the pump's operating envelope.
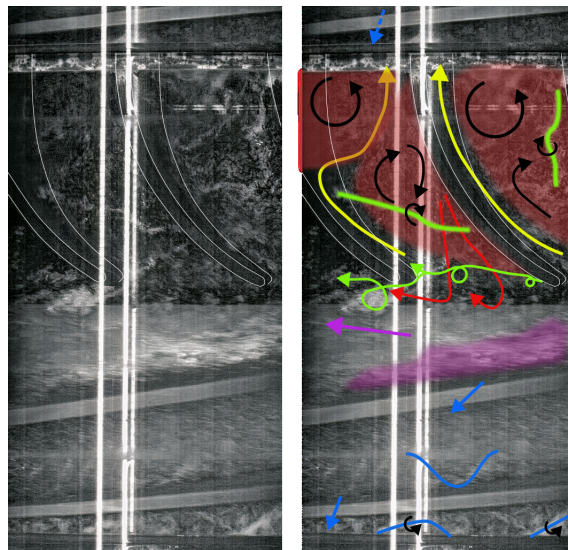

Figure 8: Flow visualization at 45% relative flow rate

Similarly to the previous operating point at 61% of BEP, the flow field was highly unsteady. Secondary flows related to the tip leakage flow dominated the flow pattern in the impeller. In the diffuser, the fluid dynamics at the inlet were similar to those at 61% of BEP, but with a higher degree of obstruction for streamwise flow. The size of the recirculating volume within the channel had increased and the reversed flow along the hub was more significant. At the diffuser outlet, there is generally only one large counterclockwise recirculation, but the streamwise flow shifts irregularly between the left and right-hand side of the vortex. A vertical vortex core can be seen along the suction side of one diffuser vane, originating from the gradient in tangential velocity between the hub and the shroud. This vortex was also identified at higher relative flow rates.
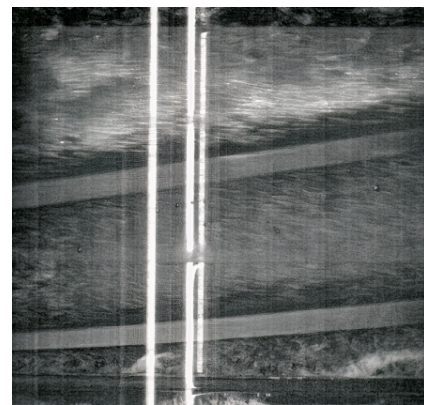
In the outlet section of the impeller, a locally higher gas volume fraction was observed near the hub and the pressure side of the impeller blade, marked with purple in figure 8. The cloud

of bubbles was nearly stagnant in the impeller, suggesting that gas bubbles had migrated to a region of very low relative velocity with a locally reduced pressure. In general, the probability of phase separation increases towards the impeller outlet, where the centrifugal force acting on the fluid is large and the balancing Coriolis force is small due to the low relative velocity. A tendency to phase separation close to the impeller trailing edge was also observed at 61% of BEP, but here the slip velocity between the phases appears insignificant. The cloud of bubbles would follow the streamwise flow out of the impeller and was dispersed in the diffuser inlet. At 45% of BEP however, the gas accumulated in a larger area, reaching further upstream, and appeared nearly stagnant.

The shift in slope in the single-phase performance characteristic seen in figure 3 can be attributed to the emergence of this region of stagnant fluid. The impeller outlet becomes partly obstructed and the compression cell is unable to further increase the head when the flow rate is lowered. For single phase operation, the region can be further studied through laser Doppler velocimetry and numerical analysis. In the present conditions, with 1.7% GVF, it is noteworthy how the head coefficient deviates from the single-phase performance at this particular relative flow rate. Another recording with a reduced GVF is therefore examined. Figure 9 shows two additional images of the impeller at 45% relative flow rate. Figure 9a exemplifies the conditions when the GVF was 0.8%, while 9b is from the same recording as figure 8.
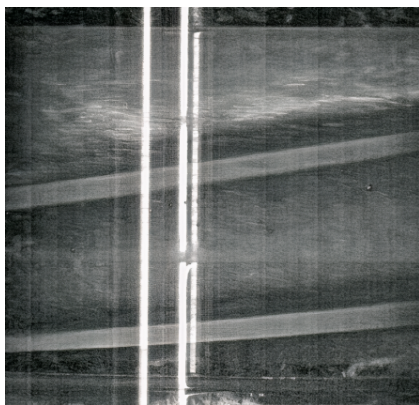
(a) Gas volume fraction of 0.8%   (b) Gas volume fraction of 1.7%

Figure 9: Examples of gas accumulation near impeller outlet at 45% relative flow rate. A small increase in inlet gas volume fraction can lead to a significantly larger region with an increased void fraction.

It is evident from figure 9 that a small increase in GVF can result in a significantly larger region where gas bubbles accumulate. At 1.7% GVF, the cloud of bubbles spreads along the hub and seemingly also the pressure side of the blade, i.e. in the spanwise direction. Note that the examples shown in figure 9 are instances of severe accumulation in each case. At 0.8% GVF, the impeller outlet channels could also exhibit very little accumulated gas. This was reflected in the pump performance, where the head coefficient was reduced by no more than 0.5% relative to single phase conditions. For the case with 1.7% GVF however, the head reduction was 1.8%, as reflected in figure 3. The head reduction is attributed to the phase separation in the impeller outlet, which escalates with higher GVF. The streamwise flow is obstructed and the locally increased void fraction reduces the impeller's ability to generate differential pressure.

CONCLUSIONS

The internal flow field in a low-specific speed helico-axial compression cell is highly unsteady and dependent on the relative flow rate. Rotor-stator interactions within the cell, as well as with upstream and downstream compression cells, determine the evolution of secondary flows at the inlet and outlet of the cell. At high relative flow rates, the flow is steady in major parts of the geometry. Nevertheless, periodic flow detachment from the hub at the diffuser inlet was observed, together with a clockwise recirculation zone at the outlet. As the flow rate is lowered towards BEP, the impeller tip leakage vortex appears and develops a serpentine shape due to the incoming flow from the diffuser. The tip leakage backflow into the diffuser is not negligible and initiates a counterclockwise recirculation zone in the diffuser outlet. At lower relative flow rates, the tip leakage flow becomes increasingly dominant and radially outwards velocity components at both pressure and suction side of the blades become prominent. The counterclockwise recirculation zones in the diffuser outlet become unstable and rearranges irregularly. The impeller inlet flow is forced to enter the impeller closer to the hub, as the shroud area is obstructed. Reversed flow along the diffuser hub results in a shear layer within the diffuser channel which leads to characteristic vortices. The reversed flow exhibits a periodicity related to the impeller blade passing frequency, especially at the lowest relative flow rates. The impellers seem then to affect each other's in and outflow conditions through the relatively short diffuser.

Secondary flows are seen to be dominant in major parts of the low-specific speed helico-axial compression cell, also when operating near the best efficiency point. The tip leakage flow is the main source for secondary flows in the impeller and the upstream diffuser outlet. Although the tip leakage flow causes substantial volumetric losses, the open impeller design eliminates the need for a front seal and avoids potential deposition and accumulation of solids. Additionally, the induced radial velocity along the impeller blade is considered to contribute positively to the redistribution and mixing of the phases. Design changes could potentially reduce the amount of recirculation and reversed flow in the diffuser. Care must however be taken to avoid promotion of phase separation when the gas volume fraction is high.

The shift in slope of the head-flow curve at very low relative flow rate can be attributed to a region of nearly stagnant fluid in the impeller outlet. Gas bubbles were observed to accumulate in this region near the hub and phase separation escalated when increasing the gas volume fraction. This lead to a reduced head compared to single phase conditions.

REFERENCES

Brennen, C. E. (2011), *Hydrodynamics of Pumps*, Cambridge University Press.

Cheng, H.-Y., Ji, B., Long, X.-P., Huai, W.-X. & Farhat, M. (2021), 'A review of cavitation in tip-leakage flow and its control', *Journal of Hydrodynamics* **33**(2), 226–242.

d'Agostino, L. (2013), On the hydrodynamics of rocket propellant engine inducers and turbopumps, *in* 'IOP Conference Series: Materials Science and Engineering', Vol. 52, IOP Publishing, p. 012004.

El Hajem, M., Vilagines, R., Champagne, J. Y. & Morel, R. (2003), Measurement of bubbly

flows inside an axial pump - a feasibility study, *in* '2nd International Conference on Heat Transfer, Fluid Mechanics and Thermodynamics'.

Gundersen, T. Ø. S., Dupoiron, M., Moënne-Loccoz, V., McAlinden, T., Juliussen, Y. C., Torbergsen, E. A., Meredith, A., Marthinussen, S.-A., Arntzen, B. J. & Hoffmann, A. C. (2022), Commissioning a new multiphase pump visualization test rig to investigate the internal flow field and its connection with pump performance, *in* 'Proceedings of the 38th International Pump Users Symposium', Turbomachinery Laboratory, Texas A&M Engineering Experiment Station.

Gundersen, T. Ø. S., Moënne-Loccoz, V. & Dupoiron, M. (2023), 'High-speed camera recordings of unsteady flow in a multistage helico-axial pump'.
URL: *https://doi.org/10.5281/zenodo.7752920*

Lakshminarayana, B. (1982), 'Fluid dynamics of inducers—a review', *Journal of Fluids Engineering* **104**(4), 411–427.

Mansour, M., Parikh, T., Engel, S., Wunderlich, B. & Thévenin, D. (2019), Investigation on the influence of an inducer on the transport of single and two-phase air-flows by centrifugal pumps, *in* 'Proceedings of the 35th International Pump Users Symposium', Turbomachinery Laboratory, Texas A&M Engineering Experiment Station.

Serena, A. & Bakken, L. E. (2015), Investigation of the blade tip clearance effects on performance and stability of a mixed-flow pump: High speed camera recordings of the flow structures, local measurements and numerical simulation, *in* 'Volume 4A: Dynamics, Vibration, and Control', American Society of Mechanical Engineers.

Tan, C. S., Day, I., Morris, S. & Wadia, A. (2010), 'Spike-type compressor stall inception, detection, and control', *Annual Review of Fluid Mechanics* **42**(1), 275–300.

Tsujimoto, Y., Horiguchi, H. & Qiao, X. (2005), Backflow from inducer and its dynamics, *in* 'Proceedings of the ASME 2005 Fluids Engineering Division Summer Meeting. Volume 1: Symposia, Parts A and B', ASME, pp. 1483–1494.

Vilagines, R., Akhras, A., Pagnier, P. & Falcimaigne, J. (2004), Average flow analysis in a multistage helico-axial pump, *in* 'The 10th International Symposium on Transport Phenomena and Dynamics of Rotating Machinery', ISROMAC. ISROMAC10-2004-065.

Vilagines, R., Pagnier, P., Akhras, A., El Hajem, M., Champagne, J. Y. & Morel, R. (2003), A study of the flow in a helical-axial pump rotor, *in* 'The 12th International Conference on Fluid Flow Technologies'.

Yamada, K., Kikuta, H., Furukawa, M., Gunjishima, S. & Hara, Y. (2013), Effects of tip clearance on the stall inception process in an axial compressor rotor, *in* 'Volume 6C: Turbomachinery', American Society of Mechanical Engineers.

Zhang, J., Cai, S., Li, Y., Zhu, H. & Zhang, Y. (2016), 'Visualization study of gas–liquid two-phase flow patterns inside a three-stage rotodynamic multiphase pump', *Experimental Thermal and Fluid Science* **70**, 125–138.